Fabrication and Characterization of Nickel Ferrite-Based Ethanol Nanosensor

Sedigheh Hoghoghifard[1] · Amin Rezaeipour[2] · Sajjad Dehghani[2]

Abstract

Ferrite nanostructures have been widely applied as effective sensing materials in detection systems for volatile organic compounds (VOCs) . This study presents a nickel ferrite ($NiFe_2O_4$) nanoparticle-based ethanol sensor which is fabricated using a simple hydrothermal technique by applying a glass substrate. The formation, structure, and physical properties of the prepared nanostructure were studied and determined by x-ray diffraction analysis, Fourier transform infrared spectroscopy, field-emission scanning electron microscopy, energy-dispersive x-ray spectroscopy, Brunauer–Emmett–Teller analysis, vibrating-sample magnetometry, and ultraviolet–visible spectroscopy. The gas sensing characteristics of the fabricated sensor were investigated under various types of analytes, different concentrations, and temperatures. The measurements demonstrated the highest response value of 195% to 100 ppm ethanol at an operating temperature of 230°C, which was much higher than the sensor's response to other analytes. Furthermore, these experiments revealed that the sensor is stable and repeatable. In summary, a low-cost fabricated sensor based on a glass substrate was evaluated at a range of temperatures (170–280°C) and ethanol concentrations (25–500 ppm). Further investigations were carried out to examine the percentage response for the fabricated sensors towards different VOCs including acetone, methanol, toluene, formaldehyde, and dichloromethane compared with ethanol.

Introduction

Nowadays, advances in industrial processes and technology are changing the human lifestyle, but are also increasing air pollution and its consequences. Therefore, gas sensors have become necessary devices to monitor environmental conditions to control the air quality. Ethanol is a clear, non-toxic, and flammable liquid that is used widely in the medical, food processing, plasticizer, plastics, and cosmetics fields.[1,2] Ethanol vapor is slightly lighter than air and is very toxic by inhalation or skin contact. Exposure to excessive concentrations of ethanol can severely harm the human body, as it targets the nervous system and affects brain function. Industrial explosions are another hidden danger of excessive ethanol concentrations. Therefore, the ability to efficiently detect these materials is essential. In recent years, nanostructures have attracted more attention as most of them are multifunctional materials with several applications.[3–10] Nanocrystalline semiconductor metal oxides are one group of these nanostructures known as resistance-type gas sensing materials.[5,11,12] These are recommended for gas detection due to their low cost, ease of synthesis, good sensitivity, and long-term stability. Recently, spinel ferrites and their composites with different structures, sizes, and morphology have been applied in biosensors, corrosion protection, drug delivery, ceramics, medical diagnostics, microwave absorbers, and transformer cores, and also in gas sensing setups to decrease working temperature and improve selectivity.[11,13,14] Among the spinel group, $NiFe_2O_4$ is a soft ferrite with an inverse spinel structure that is known as a multicomponent

✉ Sedigheh Hoghoghifard
shoghoghifard.7@gmail.com

Amin Rezaeipour
a.rezaeipour@shirazu.ac.ir

Sajjad Dehghani
sdehghani@shirazu.ac.ir

1 Department of Physics, Faculty of Science, Higher Education center of Eghlid, Eghlid 7381943885, Iran

2 Faculty of Advanced Technologies, Shiraz University, Shiraz 7194684560, Iran

oxide,[15] which motivates researchers to employ it in chemical sensing due to multiple oxidation states.[16,17]

Xu et al. synthesized porous lanthanum ferrites (LaFeO$_3$) under different pH values for ethanol gas sensing.[18] Godbole et al. proposed a gas sensor based on MgFe$_2$O$_4$ nanoparticles which showed a rapid response toward alcohol vapors.[11] In another work, Tarttelin Hernández et al. studied the gas detection efficiency of a NiFe$_2$O$_4$ sensor prepared by a levitation-jet synthesis (LJS) method.[19]

According to applied nanostructures in nanosensors, some researchers focus on ferrite-based nanocomposites. Zambare et al. proposed an effective ethanol gas sensor based on the Zn-substituted cobalt ferrite composition,[20] and Mhlongo et al. improved ethanol sensing by doping of Cr into In$_2$O$_3$ nanofibers.[21] In addition, carbon-based nanocomposites and nanostructures with a large effective surface area are considered in the fabrication of nanosensors for various gas detection applications. Nitrogen-doped carbon dots and carbon nanosheets,[22] graphene-based nanosensors,[23] and MgCo$_2$O$_4$ nanosheets[24] are examples that provide sufficient sensing active sites to improve the sensor's performance.

In the present study, building upon previous studies, we aim to synthesize nickel ferrite nanoparticles by the hydrothermal method and fabricate a stable and repeatable sensor by applying a simple method that decreases the complexity.

The prepared sensor based on NiFe$_2$O$_4$ shows a high response value, sensitivity, and selectivity to ethanol vapor.

Experimental Methods

Synthesis of NiFe$_2$O$_4$ Nanoparticles

All chemicals used herein are of analytical grade. Nickel ferrite nanoparticles were synthesized by the hydrothermal technique and calcination procedure as follows:

First, 3 mmol Fe(NO$_3$)$_3$·9H$_2$O and 6 mmol Ni(NO$_3$)$_2$·6H$_2$O were dissolved in 60 mL deionized water and stirred for 20 min at room temperature. Next, 3 M sodium hydroxide solution was added dropwise to the homogeneous reaction solution until the pH value was equal to 11. The above mixture was transferred to a 100 mL stainless steel autoclave and heated in an oven at 160°C for 12 h. After it was cooled to room temperature, the precipitate was separated and washed several times with deionized water, and then the obtained precipitate was dried at 80°C for 12 h. Finally, the as-prepared powder was calcined at 500°C for 2 h with a heating rate of 5°C/min. The synthesis procedure is shown in Fig. 1.
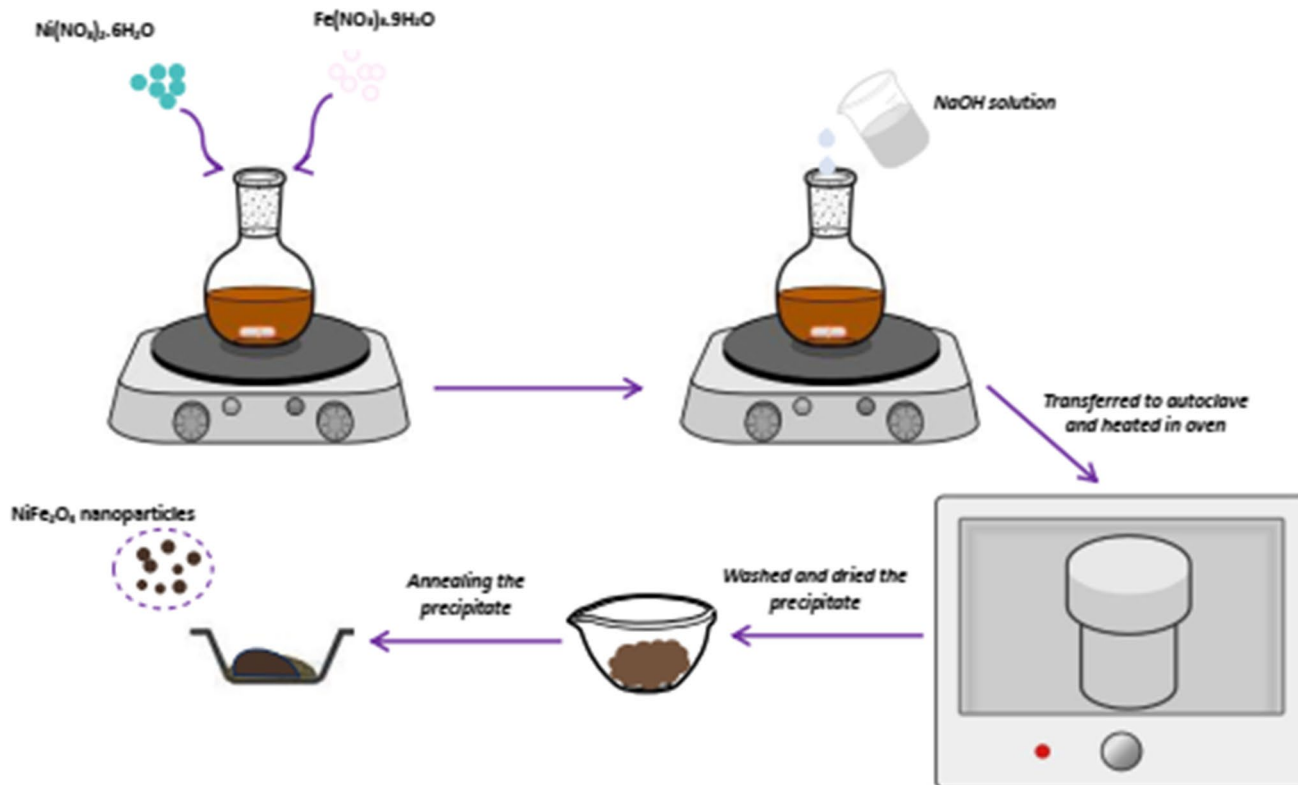

Fig. 1 The schematic diagram of the synthesis procedure.

Characterization

The crystal structure of NiFe-NP was determined by x-ray diffraction (XRD) using the D8 Advance diffractometer (Bruker, Germany) equipped with Cu-Kα radiation ($\lambda = 0.1542$ nm). The morphology was investigated through field-emission scanning electron microscopy (FESEM, TESCAN) working at an accelerating voltage of 150 kV, and the elemental composition of the synthesized sample was determined by energy-dispersive x-ray spectroscopy (EDX). Brunauer–Emmett–Teller (BET) analysis was performed using a Belsorp-mini II (MicrotracBEL Corporation) system to estimate specific area and pore size by nitrogen adsorption–desorption isotherm analysis. Vibrating-sample magnetometry (VSM) was performed to investigate the magnetic properties of the sample at room temperature using a MDKB VSM setup with an applied field up to 15 kOe. To reveal the bandgap energy of the synthesized nanoparticles, the UV–Vis spectra were obtained by a UNICO S-2150 spectrophotometer at room temperature. The Fourier transform infrared (FTIR) spectra were recorded using a PerkinElmer FTIR (Spectrum RXl) instrument.

Sensor Fabrication and Gas Sensing

The sensor fabrication procedure is described step by step as follows:

First, a thin film of nickel was deposited on a 1.5×1.5 cm^2 glass slide via the thermal evaporation method. Then, nickel ferrite nanoparticles were mixed with deionized water and homogenized using the sonication process. After that, the corresponding suspension was coated over the prepared substrate by the drop-casting method using a microsyringe. Finally, the sensor was heated over a hot plate for 10 min at 60°C to evaporate water. All sensing measurements were carried out by adjusting the sample in an 8.3 L test chamber containing two microheaters to evaporate the liquid analyte and control the sensor operating temperature. The relative humidity of the media was equal to 20%. For sensor response measurements, a given amount of the test analyte was inserted into the test chamber using a microsyringe and evaporated very rapidly. The schematic diagram of the test measurement used for testing the fabricated sensor is depicted in Fig. 2.

The sensor responses were calculated by using Eq. 1:

$$\text{Response}(\%) = (R_{\text{g}} - R_{\text{a}})/R_{\text{a}} \times 100 \tag{1}$$

Here, the air is considered as the reference gas; R_{a} is the sensor's electrical resistance in air and R_{g} represents the
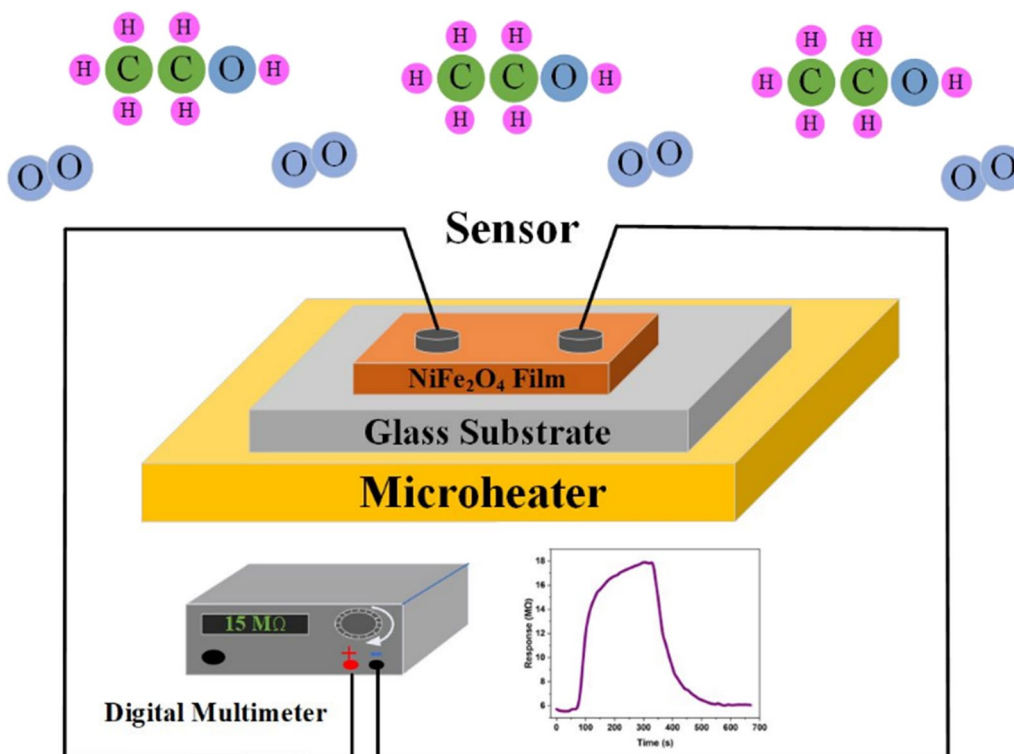

Fig. 2 The schematic diagram of the test measurement setup.

electrical resistance in the presence of the test gas. The electrical resistance was recorded by a digital multimeter (APPA-505). The response time is defined as the time taken by the sensor to reach 90% of the maximum response value.[25]

Results and Discussion

Structural Characterization

The XRD pattern (Fig. 3) identified the crystallinity, purity, and single-phase nickel ferrite that was formed in an inverse
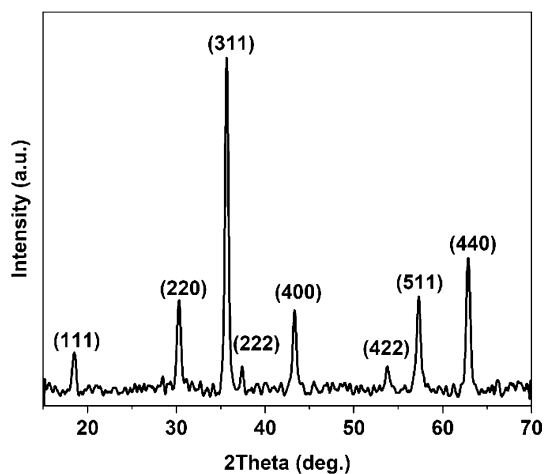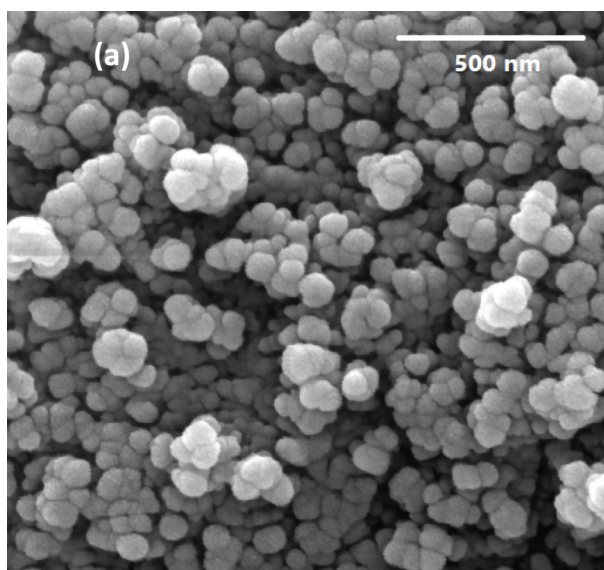
Fig. 3 XRD patterns of $NiFe_2O_4$ nanoparticles.

cubic spinel structure. The corresponding peaks were well matched to JCPDS card No. 74-2081 data.

The experimental lattice constant (a), crystallite size (D), and x-ray density ($\rho = \frac{8M}{Na^3}$) were determined by considering the angle (θ) and full width at half maximum (β) of the special peak (311), using Bragg's law and the Scherrer formula $\left(\frac{0.89\lambda}{\beta\cos\theta}\right)$.[15] The calculated values of lattice parameter, crystallite size, and x-ray density for $NiFe_2O_4$ nanoparticles annealed at 500°C are 0.836 nm, 18.2 nm, and 5.33 g/cm^3, respectively.

The FESEM images illustrate the morphology of the obtained sample. As shown in Fig. 4, the $NiFe_2O_4$ nanoparticles have an average diameter of about 65–70 nm. Furthermore, the EDX analysis result verified the high purity of the synthesized sample and the existence of nickel, iron, and oxygen with expected values.

The FTIR spectrum of $NiFe_2O_4$ nanoparticles is in the wave number range of 400–1000 cm^{-1}. The formation of nickel ferrite nanoparticles in inverse spinel structure was further identified by the FTIR spectrum. (Fig. 5 shows the FTIR spectra in the wave number range from 400 cm^{-1} to 1000 cm^{-1}). Two main peaks at 418 cm^{-1} and 598 cm^{-1} correspond to the metal-oxygen band.

The band appearing at 418 cm^{-1} is assigned to octahedral metal stretching vibrations (Fe^{3+}-O and Ni^{2+}-O) and the strong absorption band at 598 cm^{-1} corresponds to the intrinsic stretching vibration of the metal at the tetrahedral site Fe $\leftrightarrow$ O.[26,27]
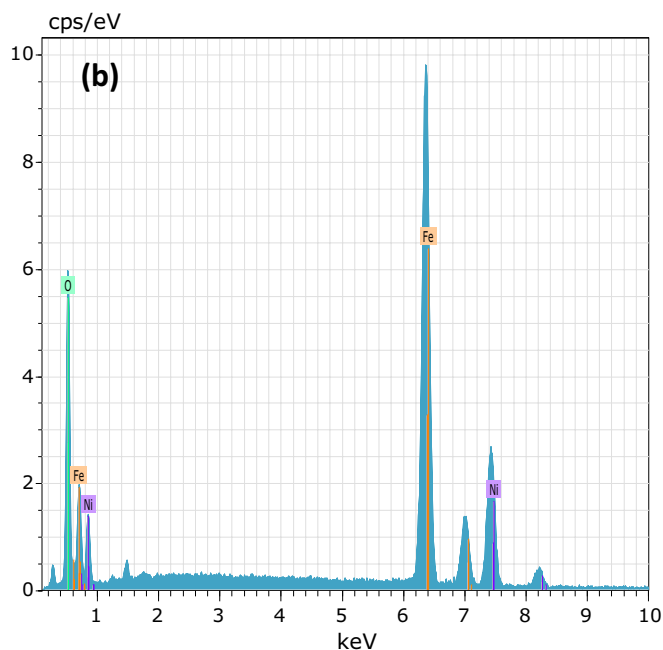
Fig. 4 (a) FESEM image, (b) EDX analysis of $NiFe_2O_4$ nanoparticles (Color figure online).
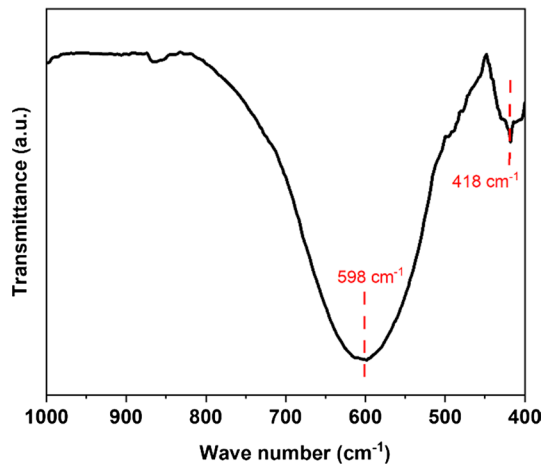
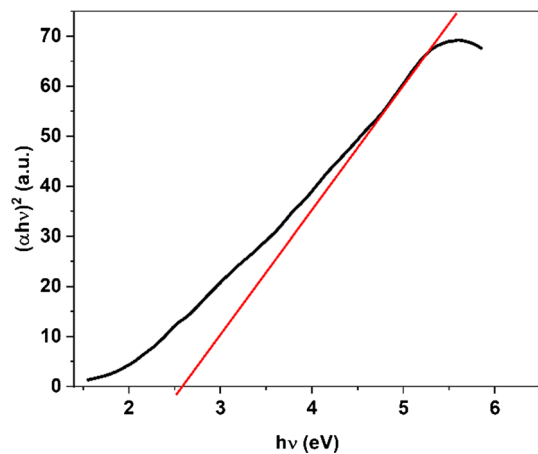Fig. 5 FTIR analysis of synthesized NiFe$_2$O$_4$ nanoparticles.

Fig. 7 N$_2$ adsorption–desorption isotherms of nickel ferrite nanoparticles.

Fig. 6 The plot of $(\alpha h\nu)^2$ versus the photon energy $(h\nu)$.

Fig. 8 Magnetization curve at room temperature.

Figure 6 illustrates the UV–Vis spectrum of NiFe$_2$O$_4$ nanoparticles. Here, with respect to the Tauc relation, the bandgap in the direct transition is calculated using Eq. 2 as follows:

$$(\alpha h\nu)^2 = (h\nu - E_g) \qquad (2)$$

where α is the absorption coefficient, h is the Planck constant, ν is the frequency of light, and E_g is the bandgap of the sample.[28] The bandgap can be estimated using the $(\alpha h\nu)^2$ versus $(h\nu)$ plot by extrapolating the straight-line region of the curves to the horizontal axis. The obtained optical bandgap value is equal to 2.58 eV.

Figure 7 shows N$_2$ adsorption–desorption isotherms for annealed nickel ferrite nanoparticles. The curve confirms that the sample belongs to type V based on the IUPAC definition and the hysteresis loop related to the mesoporous feature in the nanoparticle structure.
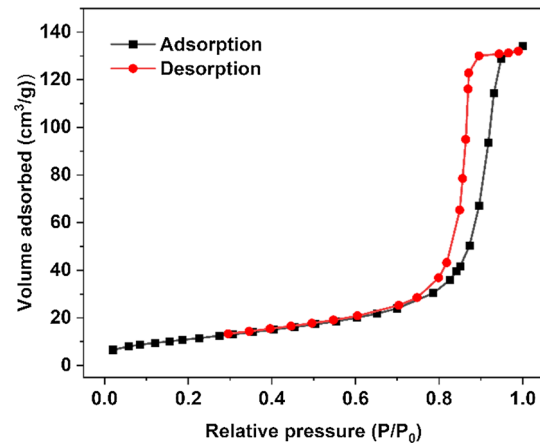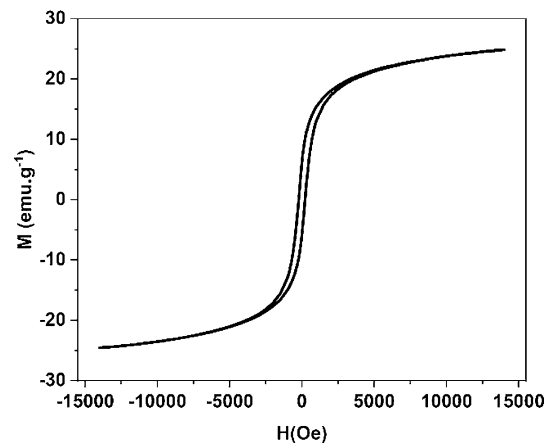
The specific area, average pore diameter, and total pore volume were calculated using the BET method as 39.75 m^{2}g^{-1}, 20.72 nm, and 0.21 cm^{3}g^{-1}, respectively.

The M-H loop obtained from VSM analysis at room temperature (300 K) is shown in Fig. 8. The magnetic hysteresis curve presents the soft ferromagnetic nature of the NiFe$_2$O$_4$ nanoparticles. The saturation magnetization (M_s), remanence magnetization (M_r), and coercivity (H_c) are 24.6 emu g^{-1}, 6.2 emu g^{-1}, and 225 Oe, respectively, as evaluated using Fig. 8.

Gas Sensing Properties

In order to study the gas sensing properties, the obtained nickel ferrite nanoparticles were applied to the gas sensor

structure. First, the sensor is examined at different temperatures in the range of 170–280°C to determine the OT as an important parameter in the sensing process, reaction kinetics, and temperature dependency behavior. As shown in Fig. 9, the sensor has a maximum response value (195%) at 230°C and 100 ppm ethanol concentration. The sensor presents increasing and decreasing behavior around the OT. Below the OT, the target gas molecules do not have enough energy to activate and overcome the energy barrier, but by increasing the temperature to the OT, the molecules gain adequate energy, leading to adsorption of more oxygen species and response enhancement. However, by increasing the operating temperature from OT, the adsorbed gas molecules may escape without reaction. To investigate the dynamic response of nickel ferrite nanoparticle-based sensors toward ethanol, the ethanol concentration was varied from 25 ppm to 500 ppm.

As expected, an increasing trend was recorded for the response values by increasing the ethanol vapor concentration, exposing the sensor to more ethanol molecules. The sensor's response at 230°C to different ethanol concentrations is presented in Fig. 9. The response and recovery time to 100 ppm ethanol are 73 s and 75 s, respectively, as shown in Fig. 9.

Figure 9d shows the response values of the sensor upon exposure to 100 ppm ethanol concentration and air for three cycles. In each cycle, after recovery and return to the initial value, we injected 100 ppm ethanol again for the next time measurement. This confirms that the present sensor is repeatable and has successful operation in ethanol sensing.

To evaluate the limit of detection (LOD), the sensor was tested from 7 ppm to 18 ppm ethanol at 230°C operating temperature, which is shown in Fig. 10. The fabricated sensor had a low order of detection (7 ppm) with a 15%
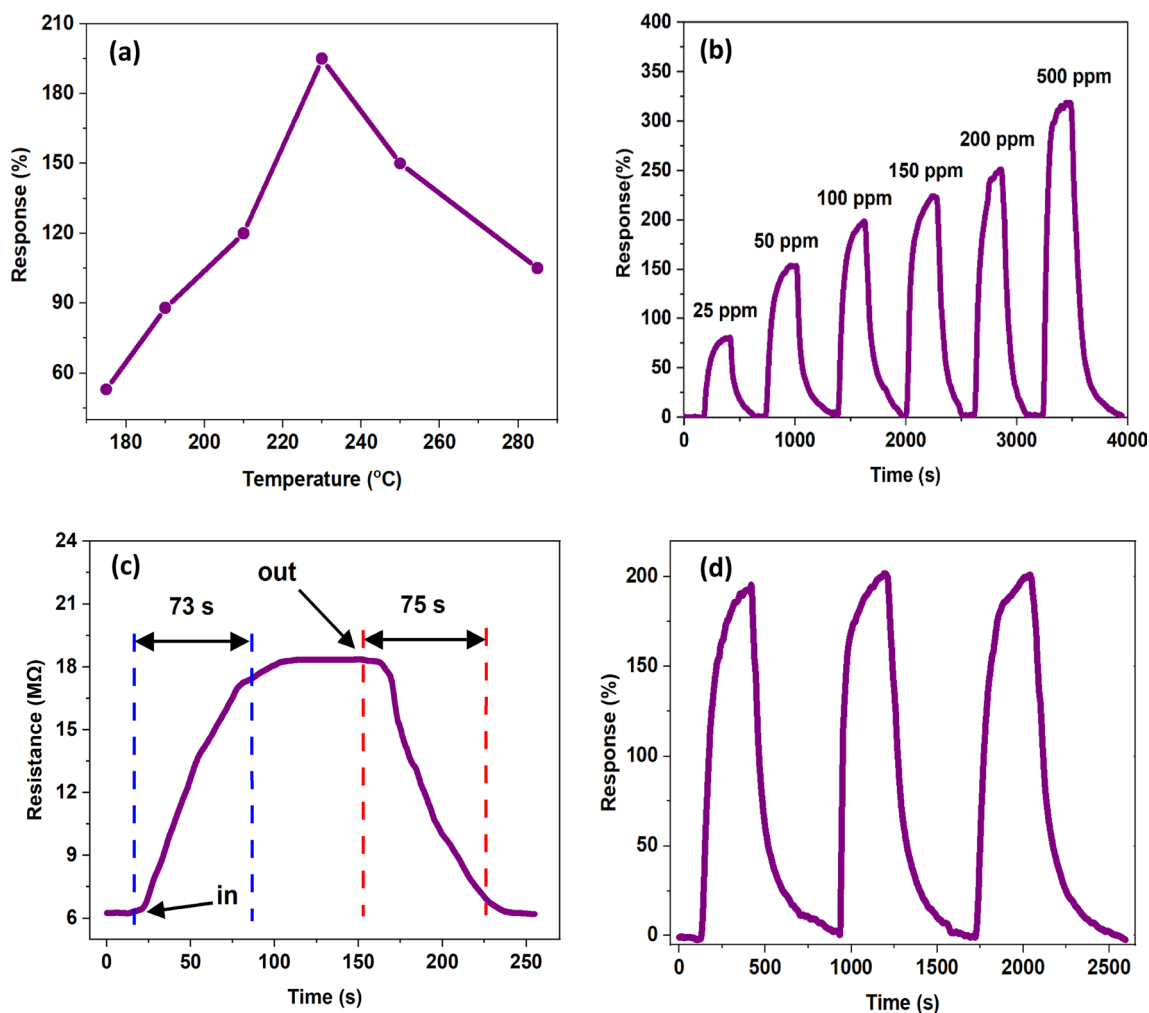
Fig. 9 (a) The response of the sensor to 100 ppm ethanol at different temperatures, (b) the response of the sensor in different ethanol concentrations, (c) the response-recovery time of the sensor, and (d) the response of sensors at their optimum temperature to three cycles of 100 ppm ethanol and air.

response. Moreover, it demonstrated a linear response in this range of ethanol concentration.

Figure 11 shows the stability of the sensor within 30 days, which is an important parameter of gas sensors. The long-term stability of the fabricated sensor was studied on the test setup when the temperature of the microheater was optimal, starting with 100 ppm ethanol until it reached a maximum and then allowed to recover and returned to the initial state. The results reveal that the sensor has long-term stability over the test period.

To examine the ability of the prepared sensor to distinguish different volatile organic compounds (VOCs), the sensor was tested at 230°C and 100 ppm ethanol (C_2H_6O), acetone ((CH_3)$_2CO$), methanol (CH_3OH), toluene (C_7H_8), formaldehyde (CH_2O) and dichloromethane (CH_2Cl_2). The sensor shows the highest response to ethanol (195%), based on the results compiled in Fig. 12. The selectivity of the prepared sensor for ethanol is obvious, whereas the response shows significant differences for other analytes. Therefore, the sensor is considered an ethanol sensor with an acceptable response.

Here, the resistance reveals an increase in the presence of ethanol, which means that the $NiFe_2O_4$ nanoparticles have *p*-type semiconductor properties. The gas sensing performance of the prepared sensor is investigated concerning the resistance change in the ethanol gas medium. This resistance variation is demonstrated by the surface charge model by considering the number of absorbed oxygen and adsorption sites on the surface of nickel ferrite nanoparticles which simplifies the reactions. In the air atmosphere, oxygen molecules are adsorbed onto the nanoparticle surfaces, leading to the ionization and formation of active oxygen species (O_2^-, O^-, and O^{2-}) by capturing electrons.[29,30] As the optimum

operating temperature of the fabricated sensor is 230°C, the chemical reaction between electrons and adsorbed oxygen occurs as follows:

$$O_{2(gas)} \leftrightarrow O_{2(ads)} \tag{3}$$

$$O_{2(ads)}^- + e^- \leftrightarrow 2O_{(ads)}^- \quad (100°C \prec T \prec 300°C) \tag{4}$$

Therefore, the electrical resistance of the *p*-type semiconductor decreases due to an increase in the number of holes accumulated in a thick layer near the ferrite surfaces. Once the sensor is exposed to a reducing gas atmosphere such as ethanol, the oxygen reacts with it, resulting in ionization via the following equation[11]:
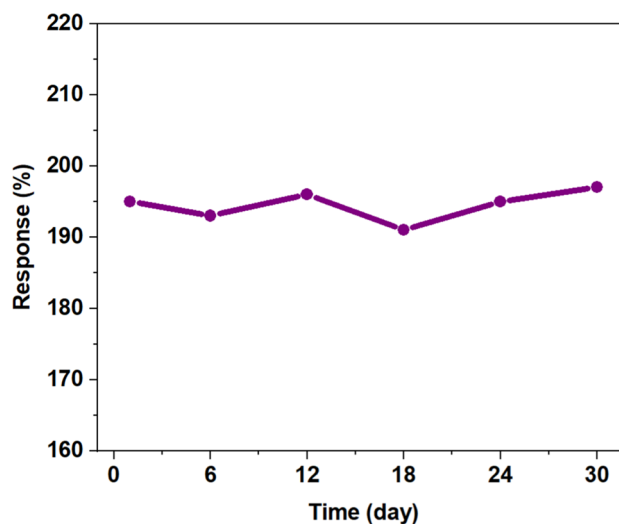
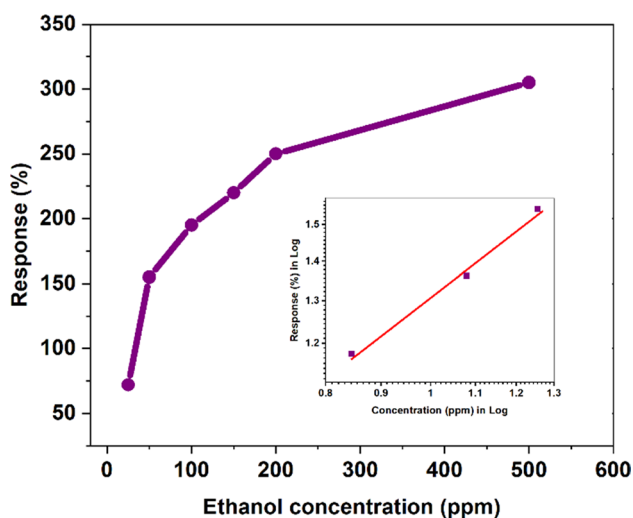**Fig. 11** Response stability over a period of 30 days upon exposure to 100 ppm ethanol.

Fig. 10 The response of the sensor to different concentrations (inset: determination the limit of detection).
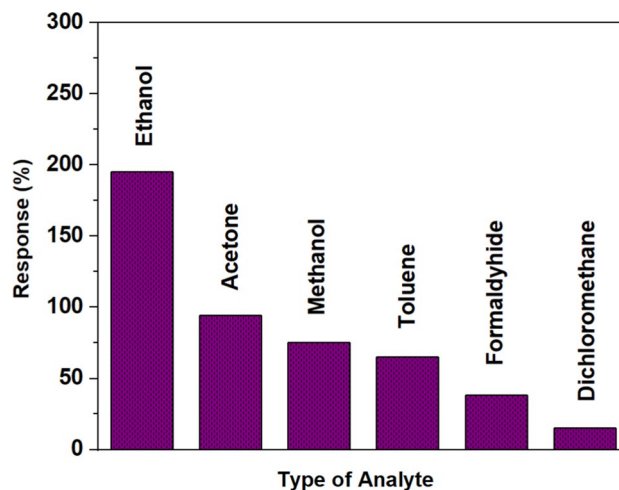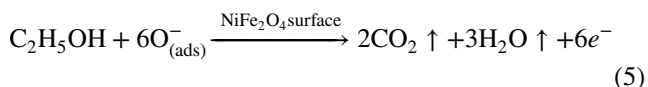
Fig. 12 Response of the sensor to different analytes with 100 ppm concentration.

$$C_2H_5OH + 6O^-_{(ads)} \xrightarrow{\text{NiFe}_2\text{O}_4\text{surface}} 2CO_2 \uparrow + 3H_2O \uparrow + 6e^-$$

(5)

Thus, the electrons produced are re-injected into the semiconductor, transferred to the conduction band, and recombined with holes in the $NiFe_2O_4$ nanostructure, which leads to an increase in the electrical resistance, as presented schematically in Fig. 13.

A comparison between this study and previous literature is presented in Table I. It can be found that our low-cost sensor which is made of uniform nickel ferrite nanoparticle thin film exhibits good sensitivity and stability at a moderate operating temperature.

Conclusions

In summary, the $NiFe_2O_4$ nanoparticle-based sensor is fabricated through a simple procedure by using a hydrothermal synthesis route. Characteristics (structural, magnetic, UV–Vis, and FTIR spectra) of the nanoparticles are discussed in detail. Based on measurements in different conditions, the sensor exhibited the highest response value (195%) to 100 ppm ethanol at 230°C. It demonstrated high sensitivity, and is capable of detecting low concentrations of ethanol (7 ppm). The response and recovery time of the sensor are 73 s and 75 s, respectively. It is worth mentioning that there is a condition in the response and recovery process because of the test setup design, whereas the fabricated sensor was tested in a real situation with the presence of air in the chamber; otherwise it could obtain much better results when the chamber was purged before the start and by using an inert gas such as argon in the chamber for the
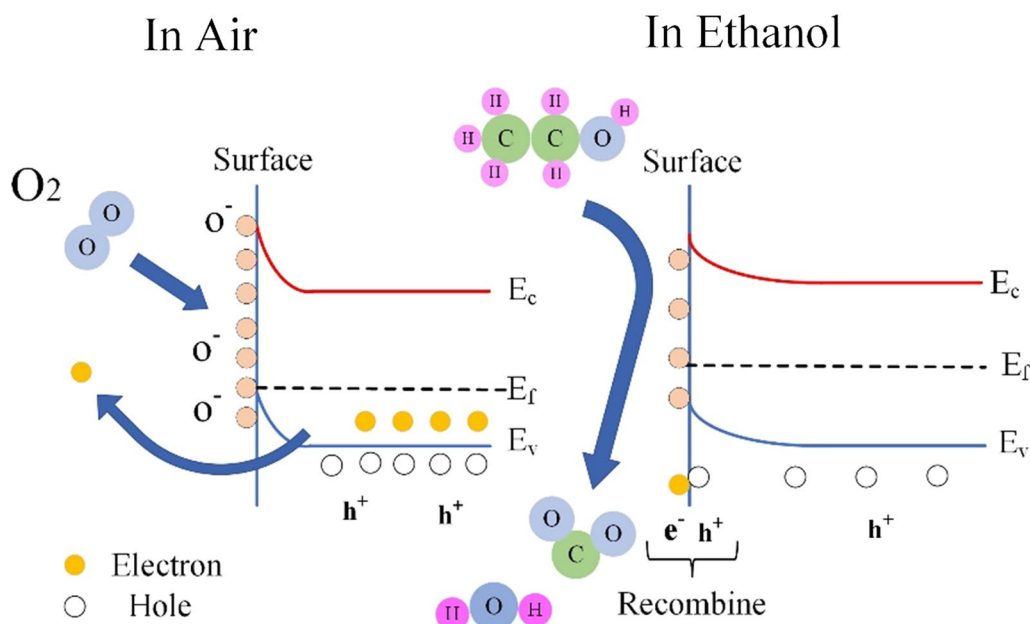

Fig. 13 Gas sensing mechanism in the studied sensor.

Table I Ethanol sensing results based on different nanostructures

Materials	Operating temperature (°C)	Ethanol concentration (ppm)	Response (%)	Ref.
$NiFe_2O_4$	375	5	200	13
$MgFe_2O_4$	275	5	73	31
$NiFe_2O_4$	300	100	21	19
Ce doped-SnO_2	375	500	44	32
Au NPs-ZnS	260	20	86.7	33
$NiFe_2O_4$	230	100	195	Present work

recovery routine. Although the response and recovery times may seem relatively high compared to some other investigations, this sensor is completely reliable for detecting ethanol in actual circumstances. In addition, the sensor shows a good response value and stability, which are the main characteristics of this device. The sensor was repeatable and can be completely recovered by exposing it to the air at its operating temperature.

Conflict of interest The authors have no known competing financial or other interests in the present study.

References

1. B. Le Daré and T. Gicquel, Therapeutic applications of ethanol: a review. *J. Pharm. Pharm. Sci.* 22, 525–535 (2019).
2. B. Strohm, *Ethanol*, in *Encyclopedia of Toxicology*, 3rd edn. (Elsevier, 2014), pp. 488–491.
3. H. Nikmanesh, S. Hoghoghifard, and B. Hadi-Sichani, Study of the structural, magnetic, and microwave absorption properties of the simultaneous substitution of several cations in the barium hexaferrite structure. *J. Alloys Compd.* 775, 1101 (2019).
4. H. Nikmanesh, S. Hoghoghifard, B. Hadi-Sichani, and M. Moradi, Erbium-chromium substituted strontium hexaferrite particles: characterization of the physical and Ku-band microwave absorption properties. *Mater. Sci. Eng. B Solid State Mater. Adv. Technol.* 262, 114796 (2020).
5. P. Halvaee, S. Dehghani, and S. Hoghoghifard, Low temperature methanol sensors based on cobalt ferrite nanoparticles, nanorods, and porous nanoparticles. *IEEE Sens. J.* 20, 4056 (2020).
6. A. Nigam and S.J. Pawar, *Structural, Magnetic, and Antimicrobial Properties of Zinc Doped Magnesium Ferrite for Drug Delivery Applications*, Ceramics International.
7. K.K. Kefeni and B.B. Mamba, *Photocatalytic Application of Spinel Ferrite Nanoparticles and Nanocomposites in Wastewater Treatment: Review*, Sustainable Materials and Technologies.
8. Y. Ai, C. Wu, G. Liu, H. Wang, C. Yao, H. Li, and Z. Li, Tuning the interfacial properties of spinels to improve the antimony adsorption ability. *Langmuir* 37, 9973 (2021).
9. J. Ma, Y. Xiong, X. Dai, and F. Yu, Zinc spinel ferrite nanoparticles as a pseudocapacitive electrode with ultrahigh desalination capacity and long-term stability. *Environ. Sci. Technol. Lett.* 7, 118 (2020).
10. Y. Xu, S. Xiang, H. Zhou, G. Wang, H. Zhang, and H. Zhao, Intrinsic pseudocapacitive affinity in manganese spinel ferrite nanospheres for high-performance selective capacitive removal of Ca^{2+} and Mg^{2+}. *ACS Appl. Mater. Interfaces* 13, 38886 (2021).
11. R. Godbole, P. Rao, and S. Bhagwat, Magnesium ferrite nanoparticles: a rapid gas sensor from alcohol. *Mater. Res. Express* 4, 025032 (2017).
12. A.T. Güntner, I.C. Weber, and S.E. Pratsinis, Catalytic filter for continuous and selective ethanol removal prior to gas sensing. *ACS Sens.* 5, 1058 (2020).
13. P. Rao, R.V. Godbole, and S. Bhagwat, Copper doped nickel ferrite nano-crystalline thin films: a potential gas sensor towards reducing gases. *Mater. Chem. Phys.* 171, 260 (2016).
14. A.B. Gadkari, T.J. Shinde, and P.N. Vasambekar, *Ethanol sensor based on nanocrystallite cadmium ferrite*, in *AIP Conference Proceedings*, Vol. 1665 (American Institute of Physics Inc., 2015).
15. S. Hoghoghifard and M. Moradi, Influence of annealing temperature on structural, magnetic, and dielectric properties of $NiFe_2O_4$ nanorods synthesized by simple hydrothermal method. *Ceram. Int.* 48, 17768 (2022).
16. S. Zhang et al., Highly-sensitivity acetone sensors based on spinel-type oxide ($NiFe_2O_4$) through optimization of porous structure. *Sens. Actuators B Chem.* 291, 266 (2019).
17. X.B. Li, S.Y. Ma, F.M. Li, Y. Chen, Q.Q. Zhang, X.H. Yang, C.Y. Wang, and J. Zhu, Porous spheres-like ZnO nanostructure as sensitive gas sensors for acetone detection. *Mater. Lett.* 100, 119 (2013).
18. Y.J. Xu et al., Magnetic behavior, photocatalytic activity and gas-sensing performance of porous lanthanum ferrites powders. *Mater. Chem. Phys.* 267, 124628 (2021).
19. P. Tarttelin Hernández, M.V. Kuznetsov, I.G. Morozov, and I.P. Parkin, Application of levitation-jet synthesized nickel-based nanoparticles for gas sensing. *Mater. Sci. Eng. B Solid State Mater. Adv. Technol.* 244, 81 (2019).
20. R.R. Powar, V.G. Parale, V.D. Phadtare, S.B. Wategaonkar, R.K. Mane, J.L. Gunjkar, D.R. Patil, P.B. Piste, H.H. Park, and D.N. Zambare, Nanocrystalline spinel zinc-substituted cobalt ferrite thick film an efficient ethanol sensor. *Mater. Today Chem.* 22, 100607 (2021).
21. M.B. Kgomo, K. Shingange, H.C. Swart, and G.H. Mhlongo, Evolution of In_2O_3 morphology from belt to fibrous-like structure for ethanol detection at low working temperature induced by Cr-addition. *Appl. Surf. Sci.* 639, 158210 (2023).
22. L.L. Mokoloko, J.B. Matsoso, N. Antonatos, V. Mazánek, B.D. Moreno, R.P. Forbes, D.H. Barrett, Z. Sofer, and N.J. Coville, From 0D to 2D: N-doped carbon nanosheets for detection of alcohol-based chemical vapours. *RSC Adv.* 12, 21440 (2022).
23. H.R. Moshayedi, M. Rabiee, and N. Rabiee, A novel graphene-based nanosensor for detection of ethanol gas. *Iran J. Sci. Technol. Trans. A Sci.* 43, 2227 (2019).
24. S. Rathinavel, S. Vadivel, and G. Balaji, Development of ethanol and acetone gas sensing performance of $MgCo_2O_4$ nanosensors by clad modified fiber optical method. *Opt. Fiber Technol.* 48, 218 (2019).
25. X. Zhu, J. Zhang, Q. Xie, and Z.L. Hou, High-sensitivity and ultrafast-response ethanol sensors based on graphene oxide. *ACS Appl. Mater. Interfaces* 12, 38708 (2020).
26. F. Majid, J. Rauf, S. Ata, I. Bibi, A. Malik, S.M. Ibrahim, A. Ali, and M. Iqbal, Synthesis and characterization of $NiFe_2O_4$ ferrite: sol-gel and hydrothermal synthesis routes effect on magnetic. *Struct. Dielectr. Charact. Mater. Chem. Phys.* 258, 123888 (2021).
27. P.D. Patil, S.R. Shingte, V.C. Karade, J.H. Kim, T.D. Dongale, S.H. Mujawar, A.M. Patil, and P.B. Patil, Effect of annealing temperature on morphologies of metal organic framework derived $NiFe_2O_4$ for supercapacitor application. *J. Energy Storage* 40, 102821 (2021).
28. S. Chakraborty and M. Pal, Highly selective and stable acetone sensor based on chemically prepared bismuth ferrite nanoparticles. *J. Alloys Compd.* 787, 1204 (2019).
29. M. Al-Hashem, S. Akbar, and P. Morris, Role of oxygen vacancies in nanostructured metal-oxide gas sensors: a review. *Sens. Actuators B: Chem.* 301, 126845 (2019).
30. A. Rezaeipour, S. Dehghani, and S. Hoghoghifard, VOC sensors based on nanoparticles and nanorods of nickel ferrite. *IEEE Sens. J.* 22, 16464 (2022).
31. V. Nagarajan, A. Thayumanavan, and R. Chandiramouli, Magnesium ferrite nanostructures for detection of ethanol vapours—a first-principles study. *Proc. Appl. Ceram.* 11, 296 (2017).

32. K. Govardhan and A. Nirmala Grace, Temperature optimized ammonia and ethanol sensing using Ce doped tin oxide thin films in a novel flow metric gas sensing chamber. *J. Sens.* **2016** (2016).

33. L. Zhang, R. Dong, Z. Zhu, and S. Wang, Au nanoparticles decorated ZnS hollow spheres for highly improved gas sensor performances. *Sens. Actuators B Chem.* 245, 112 (2017).